

Numerical study of the critical phases of the frustrated $\mathbb{Z}(5)$ model

Christophe Chatelain

Groupe de Physique Statistique, Département P2M, Institut Jean Lamour
(CNRS UMR 7198), Université de Lorraine, France

E-mail: christophe.chatelain@univ-lorraine.fr

Abstract. The phase diagram of the $\mathbb{Z}(5)$ spin model is studied numerically on the square lattice by means of the *Density Matrix Renormalization Group*. In the regime where the two nearest-neighbor couplings have opposite signs, a critical phase, not observed in earlier Monte Carlo simulations, is identified. The new phase diagram is in agreement with predictions made by M. den Nijs [*Phys. Rev. B* **31**, 266 (1985)]. All critical phases are shown to be compatible with a central charge $c = 1$. The magnetization scaling dimension displays however a different behavior in the different critical phases.

PACS numbers: 05.20.-y, 05.50.+q, 75.10.Hk, 05.70.Jk, 05.10.-a

1. Introduction

Frustration usually induces more complex, and therefore interesting, new physics. In conjunction with disorder, like in glasses for example, frustration leads, at sufficiently low temperature, to a complete freezing of the system over accessible time scales. In pure systems, in particular in magnetic systems, an increase of the degeneracy of the ground state is observed when frustration is introduced. In some cases, the ground state may even become infinitely degenerated, leading to a finite entropy per site at zero temperature. When thermally activated defects are interacting, the low-temperature phase may be critical and bounded by a Berezinskii-Kosterlitz-Thouless (BKT) topological phase transition [1, 2]. Such a situation will be considered in this paper.

Frustration can be introduced mainly in three different ways in a lattice spin model. First, a fraction of the interactions between spins can be changed in order to favor locally different ground states. A fraction of anti-ferromagnetic exchange couplings can be introduced in a ferromagnetic spin model for example. An interesting example is the fully-frustrated Ising model for which an odd number of exchange couplings are anti-ferromagnetic in each plaquette of a square lattice [3]. Consequently, the ferromagnetic phase is unstable at any finite temperature. The anti-ferromagnetic Ising model on a triangular lattice also belongs to this class of fully-frustrated models. The latter does not undergo any symmetry-breaking phase transition but a new BKT topological transition driven by the magnetic field appears [4]. Similarly, Potts [5] and XY [6] fully-frustrated models were considered. Even simpler two-dimensional models

where horizontal bonds are ferromagnetic while vertical ones are anti-ferromagnetic display interesting new phase diagrams. The 3-state Potts model on a square lattice with horizontal and vertical couplings, resp. J_h and J_v , such that $J_v \cdot J_h < 0$ undergoes a BKT transition too [7]. In three dimensions, Ding *et al.* studied a mixed Potts model with Hamiltonian [8]

$$-\beta H = K \sum_{(i,j),z} \delta_{\sigma_{i,z}, \sigma_{j,z}} - K \sum_{i,z} \delta_{\sigma_{i,z}, \sigma_{i,z+1}} \quad (1)$$

i.e. anti-ferromagnetic interactions in the z -direction and ferromagnetic ones in the two other directions. In contrast to the 2D case, they found, using Monte Carlo simulations, a second-order phase transition in the universality class of the $O(n)$ model with $n = q - 1$ and, when $q \geq 4$, a discontinuous phase transition to a phase with a different type of long-range order.

The second manner to induce frustration in lattice spin models is to add next-nearest neighbor interactions. The most celebrated model of this kind is the ANNNI model [9]. In 2D, its phase diagram displays a critical phase between the ferromagnetic and paramagnetic phases. The three phases are separated by two BKT transitions. In 3D, a so-called Lifshitz multicritical point lies at the meeting of the two transition lines. Similarly, a 2D 3-state Potts model with competing interactions between nearest and next-to-nearest neighbors was studied by den Nijs [10]. The phase diagram displays a critical phase, where the ground state and the thermally activated defects can be mapped onto a 8-vertex model. The critical exponents were inferred from this mapping.

The third and less studied manner to induce frustration is to introduce two different interactions between each pair of nearest neighbors of the lattice. Lee and Grinstein considered the generalized XY model with Hamiltonian [11]:

$$-\beta H = \sum_{(i,j)} [J_1 \cos(\theta_i - \theta_j) + J_2 \cos(2\theta_i - 2\theta_j)] \quad (2)$$

where $\theta_i \in [0; 2\pi[$. Besides the vortices giving rise to the usual BKT transition, they found half-integer vortices and string excitations. The phase diagram displays lines of BKT transitions and lines of Ising transitions. Dian *et al.* considered the Lee-Grinstein model with $J_2 < 0$ and found an additional spin-ice phase [12]. Poderoso *et al.* extended this model to [13]

$$-\beta H = \sum_{(i,j)} [\Delta \cos(\theta_i - \theta_j) + (1 - \Delta) \cos(q\theta_i - q\theta_j)]. \quad (3)$$

It was later shown that for $q = 3$ the Ising line is replaced by a line in the universality class of the 3-state Potts model [14]. The $\mathbb{Z}(q)$ model that will be considered in this paper is a discretized version of the Lee-Grinstein model [15]:

$$-\beta H = \sum_{(i,j)} \left[J_1 \cos \frac{2\pi}{q} (\sigma_i - \sigma_j) + J_2 \cos \frac{4\pi}{q} (\sigma_i - \sigma_j) \right]. \quad (4)$$

where $\sigma_i \in \{0 \dots q-1\}$. den Nijs discussed the phase diagram and proposed a scenario for the sequence of transitions undergone by the model [16]. The phase diagram of the $\mathbb{Z}(5)$ model (including the anti-ferromagnetic regime $J_1 < 0$) was shortly after determined numerically by Monte Carlo simulations [17]. While the ferromagnetic

regime $J_1 > 0$ is well reproduced by the numerical data, discrepancies with den Nijs' predictions were observed in the anti-ferromagnetic regime. The accuracy was further improved by later numerical studies of the ferromagnetic regime [18], but, as far as we are aware, the anti-ferromagnetic regime has not been studied in the last three decades. A much more accurate test of den Nijs' predictions is now possible.

In the following, a numerical study of the phase diagram of the $\mathbb{Z}(5)$ model is presented. In section 2, known results concerning this model are briefly summarized and den Nijs' interpretation of the mechanism of the transitions is presented. In section 3, different observables, numerically computed, are discussed to determine the phase diagram. Discrepancies are found with earlier Monte Carlo simulations. The nature of the phase transitions in the regime $J_1 < 0$ is then studied by considering the lattice size behavior at some particular values of the coupling J_1 . Helicity modulus and entanglement entropy are considered. Finally, the magnetization scaling dimension is estimated by a log-log fit of spin-spin autocorrelation functions. Conclusions follow.

2. The $\mathbb{Z}(5)$ model and its phase diagram

We consider the lattice spin model defined by the following Hamiltonian:

$$-\beta H = \sum_{(i,j)} \left[J_1 \cos \frac{2\pi}{q} (\sigma_i - \sigma_j) + J_2 \cos \frac{4\pi}{q} (\sigma_i - \sigma_j) \right] + h \sum_i \cos \frac{2\pi}{q} \sigma_i \quad (5)$$

with $q = 5$. The spin σ_i lies on the i -th node of a square lattice. The first two terms couple the pairs (i, j) of nearest-neighbors on the lattice. Both favor a ferromagnetic ordering when J_1 and J_2 are positive. Frustration is induced if $J_1 J_2 < 0$. The last term is the Zeeman Hamiltonian coupling the spins with an external magnetic field. While the other terms are invariant under any cyclic permutation of the q states, i.e. under the transformations of the group $\mathbb{Z}(q)$, the Zeeman Hamiltonian breaks this symmetry. The definition of magnetization $M = \sum_i \langle \cos \frac{2\pi}{q} \sigma_i \rangle$ is immediately implied by the Zeeman Hamiltonian. In the following, we will restrict ourselves to the case $h = 0$ in the bulk of the system. Magnetic fields will only be applied at the boundaries.

For $J_2 = 0$, one recovers the 5-state clock model [19]. Along this line, the ferromagnetic and paramagnetic phases are separated by a thin critical phase, bounded by two BKT phase transitions. For $J_1 = J_2$, one can check that the Hamiltonian reduces to

$$-\beta H = J \sum_{(i,j)} \left[2\delta_{\sigma_i, \sigma_j} - \frac{1}{2}(1 - \delta_{\sigma_i, \sigma_j}) \right] = J \sum_{(i,j)} \left[\frac{5}{2}\delta_{\sigma_i, \sigma_j} - \frac{1}{2} \right] \quad (6)$$

i.e. the 5-state Potts model [19]. Therefore, the system undergoes a weak first-order phase transition for $J_1 = J_2 = \frac{2}{5} \ln(1 + \sqrt{5}) \simeq 0.470$. The self-duality of the Potts model can be extended to the case $J_1 \neq J_2$ [15, 20]. Introducing the two parameters

$$x_1 = e^{\mu_1 J_1 + \mu_2 J_2}, \quad x_2 = e^{\mu_1 J_2 + \mu_2 J_1} \quad (7)$$

where

$$\mu_1 = \cos \frac{2\pi}{5} - 1 = \frac{\sqrt{5} - 5}{4}, \quad \mu_2 = \cos \frac{4\pi}{5} - 1 = -\frac{\sqrt{5} + 5}{4} \quad (8)$$

the line of self-duality is given by

$$x_1 + x_2 = \frac{\sqrt{5} - 1}{2}. \quad (9)$$

The system undergoes a single phase transition along a finite portion of this self-dual line that is delimited by the two Fateev-Zamolodchikov points where the model is integrable by algebraic Bethe ansatz [21]. The transition point of the Potts model ($J_1 = J_2$) belongs to this portion of the self-dual line. Between the two Fateev-Zamolodchikov points, the transition is of first-order while it is of second order at these points. Outside of this finite portion of the self-dual line, the system undergoes two BKT transitions and the self-dual line is in the critical phase. The clock model $J_2 = 0$ corresponds to this situation. A second branch of the self-dual line is in the region $J_1 < 0$ and $J_2 > 0$. According to earlier Monte Carlo simulations, the line lies in a critical phase [17].

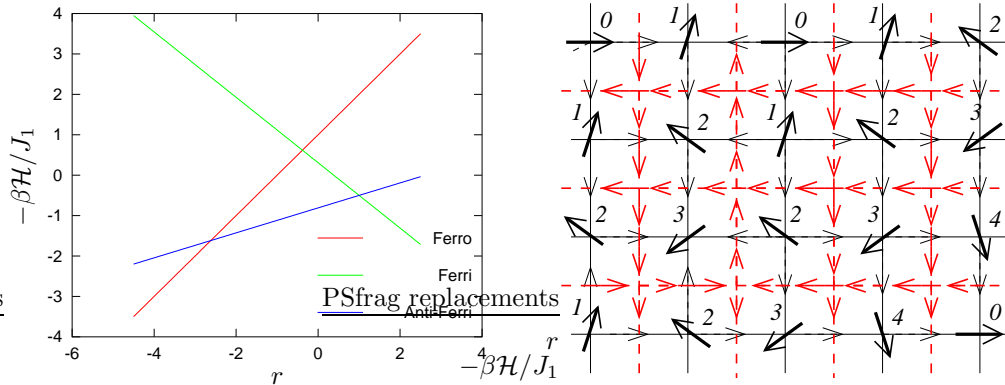


Figure 1. On the left, reduced values $-\beta H / J_1$ of the energy of a bond between two spins versus $r = J_2 / J_1$. The different curves corresponds to the three possible relative states 0, 1 or 2 of the spins $|\sigma' - \sigma| \bmod q$. On the right, example of a spin configuration in the ferrimagnetic phase in the limit $J_1 \rightarrow \pm\infty$. The spins are represented as bold black arrows. Light black arrows are the bond variables d_{ij} and the red arrows at the center of each plaquette correspond to the equivalent six-vertex ice model.

The phase diagram is readily obtained in the two limits $J_1 \rightarrow \pm\infty$. As discussed for instance in Ref. [17], the energy βH of the bond connecting the two spins σ and σ' takes only three possible values :

$$-\beta H = \begin{cases} J_1 + J_2 & (\sigma = \sigma') \\ aJ_1 + bJ_2 & (\sigma = \sigma' \pm 1 \bmod q) \\ bJ_1 + aJ_2 & (\sigma = \sigma' \pm 2 \bmod q) \end{cases} \quad (10)$$

where $a = \cos \frac{2\pi}{5}$ and $b = \cos \frac{4\pi}{5}$. Using a magnetic language, the first case corresponds to a ferromagnetic state, the second to a ferrimagnetic one and the third to an anti-ferrimagnetic state. On figure 1, the different energies $-\beta H / J_1$ are represented with respect to $r = J_2 / J_1$. In the limit $J_1 \rightarrow +\infty$, the ground state is given by the maximum of $-\beta H / J_1$. The ground state is therefore ferromagnetic for $r > r_* = (1 - a) / (b - 1) \simeq -0.382$ and ferrimagnetic otherwise. In the limit $J_1 \rightarrow -\infty$, the ground state is given by the minimum of $-\beta H / J_1$. For $r > 1$, the ground state is ferrimagnetic. For $r < 1 / r_* = (b - 1) / (1 - a) \simeq -2.618$, the ferromagnetic state is stabilized by the positive coupling J_2 which is larger than $|J_1|$. Between these two phases, i.e. for $r \in [1 / r_*; 1]$, the ground state is anti-ferrimagnetic.

In the absence of external magnetic field, the ferromagnetic phase is q -fold degenerated. In contrast, the ferrimagnetic and anti-ferrimagnetic ground states are infinitely degenerated. Consider for example the spin configuration in the ferrimagnetic phase presented on figure 1. The spins are represented as black bold arrows located on the sites of the square lattice and making an angle $\theta_i = \frac{2\pi}{5}\sigma_i$ with the x -axis. The Potts states σ_i associated to each spin orientation is written by the side of the arrow. In the ferrimagnetic ground state, the difference between two neighboring spins σ_i and σ_j is expected to be $\sigma_i - \sigma_j = \pm 1 \pmod{q}$. The infinite degeneracy of the ground state comes from the fact that, if three spins of a square plaquette are already fixed, there still exists two possibilities for the fourth one if its two neighbors are in the same state.

It is useful to consider the bond variables $d_{ij} = \sigma_i - \sigma_j \pmod{q}$. As mentioned above, $d_{ij} = \pm 1$ in the ground state of the ferrimagnetic phase. By construction, the d_{ij} are constrained by the condition $\sum_{(i,j) \in \square_\alpha} d_{ij} = 0 \pmod{q}$ around each plaquette \square_α of the lattice. In the ferrimagnetic ground state, this condition can only be satisfied if, around each plaquette, $d_{ij} = +1$ for two of the four bonds and $d_{ij} = -1$ for the two others. The circulation $\sum_{(i,j)} d_{ij}$ vanishes for all plaquettes. On figure 1, the bond variables $d_{ij} = \sigma_i - \sigma_j \pmod{q}$ between each neighboring spins σ_i and σ_j are represented as light black arrows at the center of the lattice bond joining the two spins. As a convention, the arrow points towards the spin which is larger by 1 (modulo q) than the other one. In the ferrimagnetic (as well as anti-ferrimagnetic) ground state, there are six possible arrow configurations compatible with the constrain of a vanishing circulation. In the thermodynamic limit, there are an infinite number of ways of piling-up these plaquettes, and therefore an infinite number of possible spin configurations in the ground state. As pointed out by den Nijs [16], the configuration of these arrows can be interpreted as the height differences $h_i - h_j$ of a restricted Solid-On-Solid model (RSOS). At finite J_1 , the phase is critical due to the proliferation of massless spin wave excitations. The same conclusions can be drawn for the anti-ferrimagnetic phase, the only difference being that the difference between two neighboring spins σ_i and σ_j is expected to be $d_{ij} = \pm 2$. Following den Nijs, double arrows will be drawn on the bond joining the two spins σ_i and σ_j .

The arrow configurations in the limit $|J_1| \rightarrow +\infty$ can be mapped onto a 6-vertex model. Such a mapping, mentioned by den Nijs in the case of the $\mathbb{Z}(q)$ model, was recently described for the ground state of the Lee-Grinstein model [12]. Consider again the spin configuration in the ferrimagnetic ground state depicted on figure 1. The dual lattice is represented as red (or light gray) dashed lines. The sites of this dual lattice lie at the center of the plaquettes of the original square lattice. Each one of the four bonds emerging from any site of the dual lattice crosses one of the four bonds of the plaquette. Above, these bonds of the original lattice were given an orientation according to the sign of the difference d_{ij} of the two spins at their edges. In the following, an orientation will also be given to the bonds of the dual lattice. Consider one site of the dual lattice. Follow one of the bonds emerging from this site. Eventually, a bond of the original lattice will be crossed. Determine its orientation. If the latter corresponds to the trigonometric orientation around the plaquette, an arrow pointing outwards is placed on the bond of the dual lattice. In the other case, the arrow is inwards. As can be observed on figure 1, this set of arrows on the dual lattice, denoted $d_{\alpha\beta}^*$, corresponds to a configuration of the 6 vertex model. In particular, as a consequence of the constrain of vanishing circulation $\sum_{(i,j) \in \square_\alpha} d_{ij} = 0$, the ice rule

is satisfied: two inwards and two outwards arrows meet at each site of the dual lattice. While the bond variables d_{ij} are irrotational, their duals $d_{\alpha\beta}^*$ are divergenceless. Since $d_{ij} \rightarrow d_{\alpha\beta}^*$ is a one-to-one mapping, the degeneracy of the ground state is the same for the $\mathbb{Z}(q)$ model and the 6-vertex model at the ice point, up to a factor q corresponding to the state of the first spin. Therefore, the entropy per site takes the exact value $\frac{3}{2} \ln \frac{4}{3}$ [22]. The same discussion applies to the anti-ferrimagnetic phase, apart from the fact that $d_{ij} = \pm 2$ and therefore $d_{\alpha\beta}^* = \pm 2$ too.

As confirmed by Monte Carlo simulations, the model undergoes a phase transition from the (anti)-ferrimagnetic phase to the paramagnetic one at finite J_1 [17]. The question of the mechanism of these phase transitions is not settled. The scenario described in the following was considered as the “more likely” by den Nijs. In the ferrimagnetic phase (or floating phase), consisting only of single arrows in the limit $|J_1| \rightarrow +\infty$, local defects are excited at finite J_1 . On the square lattice, they consist of one bond with a bond variable $d_{ij} = \pm 2$. Such a defect should occur with a probability $\sim e^{J_1(1-r)(b-a)}$. The constrain of a vanishing circulation, $\sum_{(i,j) \in \square_\alpha} d_{ij} = 0$, cannot be satisfied with one bond $d_{ij} = \pm 2$ and three $d_{ij} = \pm 1$. However, the $\mathbb{Z}(q)$ symmetry allows to consider plaquettes with $\sum_{(i,j) \in \square_\alpha} d_{ij} = \pm q$ which is obviously satisfied with one bond $d_{ij} = +2$ and three $d_{ij} = +1$ (or one -2 and three -1). These local defects play the role of vortices with topological charges $+q$ and $-q$, depending on their total flux. The excited bond $d_{ij} = \pm 2$ being shared between two plaquettes, two $\pm q$ vortices are simultaneously formed. Defects consisting of plaquettes with two excited bonds, either identical, as $\{+1, -1, +2, -2\}$ and $\{+1, -1, 0, 0\}$, or different $\{-1, -1, +2, 0\}$ may also appear but with a smaller probability ‡. All of them have a vanishing circulation (or vorticity). In contrast to the $\pm q$ -vortices which are found only by pairs, these 0-vortices exist only as strings. The different 0-vortices forming these strings are connected by their excited bonds. The strings either form loops or are terminated by two $\pm q$ -vortices at each edge. den Nijs explained the phase transition between the critical ferrimagnetic phase and the paramagnetic phase, not as the unbinding of $+q$ and $-q$ -vortices as in a usual BKT transition, but as the melting of the string connecting vortices. In the anti-ferrimagnetic phase, for which all bonds variables are $d_{ij} = \pm 2$ in the ground state, local defects correspond to pairs of plaquettes with one bond with $d_{ij} = \pm 1$. Again, these defects have a circulation $\pm q$. As in the ferrimagnetic phase, defects consisting of plaquettes with two excited bonds, for example $d_{ij} \in \{+2, -2, +1, -1\}$ or $d_{ij} \in \{+2, -2, 0, 0\}$, and therefore with a vanishing circulation (or vorticity), may also appear but with a smaller probability. They form strings connecting the $\pm q$ -vortices. The melting of these strings leads to the topological transition between the anti-ferrimagnetic and paramagnetic phases.

As already mentioned in the introduction, the half-plane $J_1 > 0$ of the phase diagram is well-known and accurate numerical results can be found in the literature. In contrast, the case $J_1 < 0$ was not studied in the last three decades and is not known with a good accuracy. Up to now, den Nijs’ proposed phase diagram is not confirmed by Monte Carlo simulations.

‡ respectively $e^{2J_1(1-r)(b-a)}$, $e^{2J_1[1-a+(1-b)r]}$ and $e^{J_1[(1+b-2a)+(1+a-2b)r]}$.

3. Numerical results

We studied numerically the $\mathbb{Z}(5)$ model using the algorithm *Density Matrix Renormalization Group* [23, 24] (DMRG). The ground state of the transfer matrix is expressed as a matrix product state of two blocks, left and right. In the determination of the phase diagram, these two blocks were allowed to grow up to 325 states. This number of states was increased for the small subset of points where the diagonalization routine failed to converge. The ground state, first obtained by the Infinite-Size DMRG algorithm, was refined using six sweeps of the Finite-Size DMRG algorithm. The phase diagram was constructed by performing calculations for the lattice size $L = 128$ for 60 different values of J_1 and 60 of J_2 . Additional simulations for lattice sizes $L = 32, 48, 64$ and 96 at some potentially interesting values of J_1 were then performed.

3.1. DMRG estimation of the phase diagram

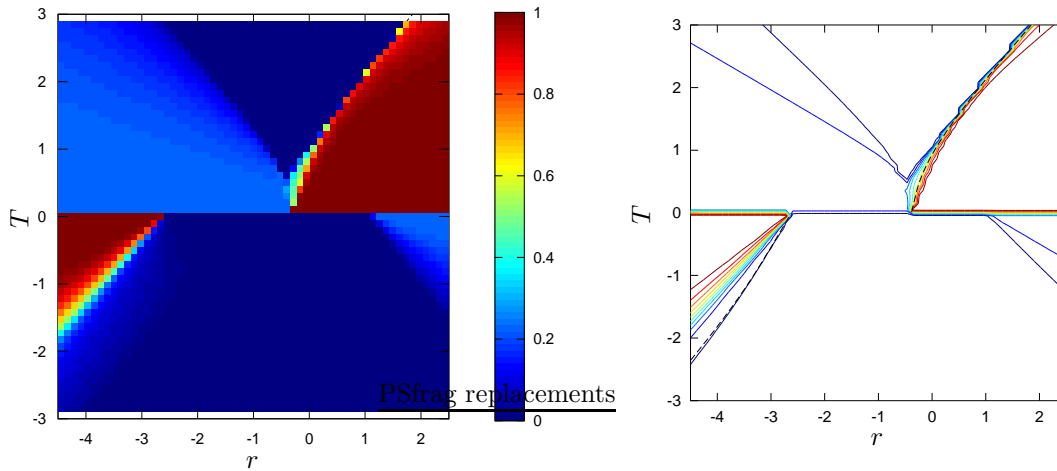


Figure 2. Magnetization $\langle \cos \frac{2\pi}{5} \sigma_{L/2} \rangle$ versus $r = J_2/J_1$ and $T = 1/J_1$ for a lattice size $L = 128$ obtained by DMRG with 325 states and 6 sweeps. On the right, contour plot of the same data. The dashed line is the self-dual line of the model.

The two ferromagnetic phases are easily localized using the local magnetization $m = \langle \cos \frac{2\pi}{5} \sigma_{L/2} \rangle$ measured at the center of the chain (Figure 2). To break the $\mathbb{Z}(5)$ -symmetry and induce a non-vanishing spontaneous magnetization in these ferromagnetic phases, magnetic fields were introduced at the boundaries of the system with the Hamiltonian

$$-\beta H_{\text{BC}} = \cos \frac{2\pi}{q} \sigma_1 + \cos \frac{2\pi}{q} \sigma_L. \quad (11)$$

The convergence of the DMRG algorithm is also improved by these boundary magnetic fields. As expected, the ferromagnetic phases extend over the interval $r = J_2/J_1 \in]-\infty; -2.618]$ when $J_1 \rightarrow -\infty$ and $[-0.382; \infty[$ when $J_1 \rightarrow +\infty$. The location of the phase boundaries are in good agreement with earlier Monte Carlo simulations. In the contour plot of figure 2, one can observe that the contour line of smallest magnetization

is close to the self-dual line, apart in the region between $r \simeq -0.382$ and the first Fateev-Zamolodchikov point at $r = (\sqrt{5} - 1)/2 \simeq 0.618$ where there exists a critical phase between the paramagnetic and ferromagnetic phases. In our numerical data, the critical phase manifests itself as a broadening of the region where magnetization displays a significant variation. Note that for very negative values of r , i.e. in the region $r \lesssim -3$, a region that has not been considered numerically before, a much stronger broadening is observed. On figure 2, the phase boundary does not appear sharp but spread over an interval of values of r growing with $|J_1|$. It is tempting to conjecture that a critical phase also lies between the ferromagnetic and paramagnetic phase in the lower half-plane. This point will be discussed again in the following. Ferrimagnetic phases can also be observed, and distinguished from the ferromagnetic phases, since they display a small but non-vanishing spontaneous magnetization. In the upper-half plane $J_1 > 0$, the phase boundary with the paramagnetic phase is in fairly good agreement with Ref. [17]. In contrast, the agreement is quite poor in the lower half-plane. Last, the anti-ferrimagnetic phase is invisible to magnetization.

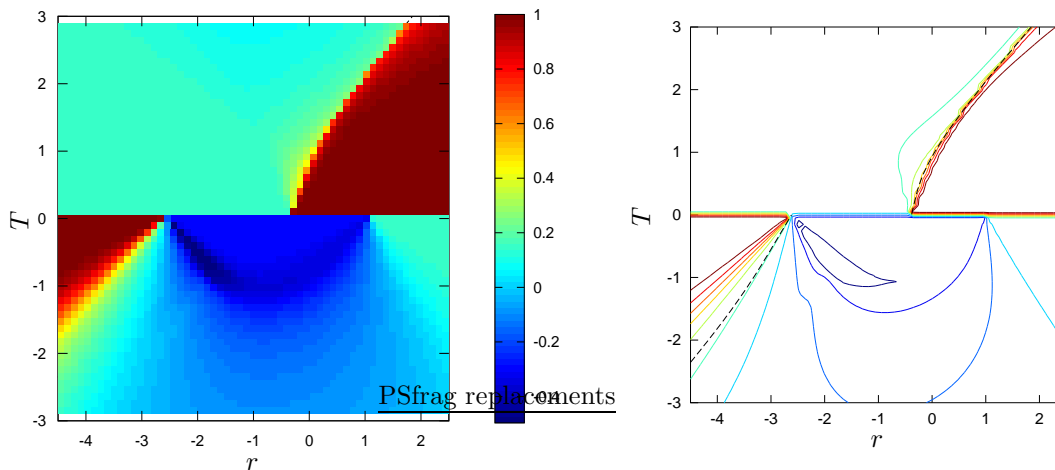


Figure 3. Magnetization-magnetization autocorrelation function A_1 versus $r = J_2/J_1$ and $T = 1/J_1$ for a lattice size $L = 128$ obtained by DMRG with 325 states and 6 sweeps. On the right, contour plot of the same data. The dashed line is the self-dual line of the model.

Another quantity that can be computed to identify the magnetic order in the system is the magnetization-magnetization autocorrelation function

$$A_1 = \langle \cos \frac{2\pi}{5} \sigma_{L/2}(1) \cos \frac{2\pi}{5} \sigma_{L/2}(0) \rangle \quad (12)$$

where the central local magnetization is measured at two successive times t . In this context, the time direction corresponds to the transverse direction of the transfer matrix. As can be seen on figure 3, the two ferromagnetic phases appear distinctly, as well as the anti-ferrimagnetic phase in the lower half-plane $J_1 < 0$. The two ferrimagnetic phases are now hardly distinguishable from the paramagnetic phase. It is however difficult to estimate the precise location of the phase boundary of the anti-ferrimagnetic phase with the paramagnetic one. Since A_1 vanishes in a purely paramagnetic phase while $A_1 = \cos \frac{4\pi}{5} \simeq -0.81$ in an anti-ferrimagnetic phase in

the limit $J_1 \rightarrow -\infty$, this phase boundary may be estimated as the location of the points where $A_1 \simeq -0.4$. The corresponding curve can be seen on the contour plot of figure 3. Of course, the choice of the value -0.4 introduces some arbitrariness. As seen on the figure, small changes to this value lead to a quite different contour plot. Nevertheless, it seems clear that the anti-ferrimagnetic phase is bounded and not infinite, in contrast to what was suggested by Monte Carlo simulations. Moreover, it does not share any common boundary with the ferromagnetic phase, apart from the point $r \simeq -2.618$ when $J_1 \rightarrow -\infty$, as stated by Ref. [17]. This discrepancy is important: den Nijs' proposal was rejected by Ref. [17] because of the observation in the Monte Carlo simulations of a common phase boundary between the ferromagnetic phase and the anti-ferrimagnetic one in the half-plane $J_1 < 0$. The absence of any common phase boundary, as observed in our DMRG calculations, is in agreement with den Nijs' proposal.

Moreover, the critical phase between the ferromagnetic and paramagnetic phases appear distinctly in yellow color ($A_1 \simeq 0.4$). Figure 3 confirms that a critical phase lies at the boundary of the ferromagnetic phase, not only in the upper half-plane J_1 but also in the lower one. In the latter, it does not seem to exist any region where the two BKT transitions merge into a single transition.

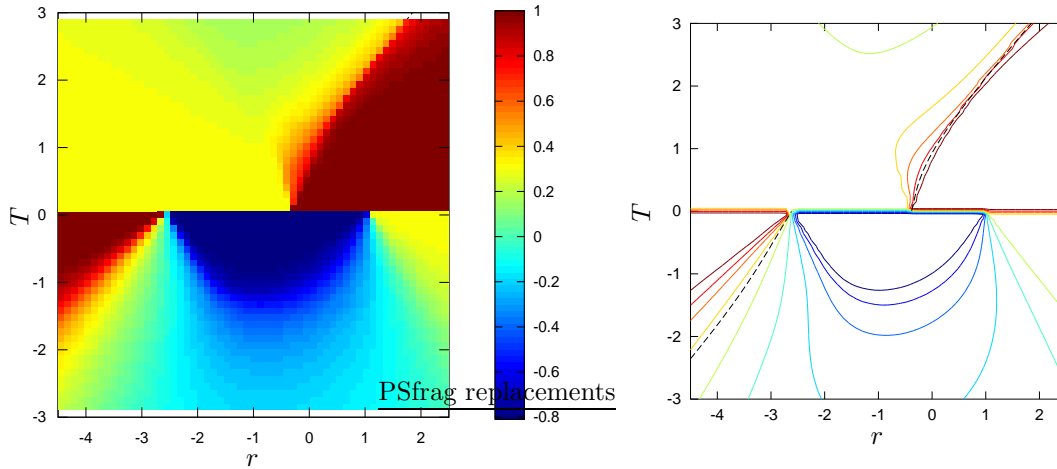


Figure 4. Two-site correlation $\langle \cos \frac{2\pi}{5} (\sigma_{L/2} - \sigma_{L/2+1}) \rangle$ versus $r = J_2/J_1$ and $T = 1/J_1$ for a lattice size $L = 128$ obtained by DMRG with 325 states and 6 sweeps. On the right, contour plot of the same data. The dashed line is the self-dual line of the model.

A closely-related observable allowing to distinguish the different phases is the nearest-neighbor spin-spin correlation

$$e = \langle \cos \frac{2\pi}{q} (\sigma_{L/2} - \sigma_{L/2+1}) \rangle. \quad (13)$$

again measured at the center of the chain. In the limit $|J_1| \rightarrow +\infty$, e is expected to take the values 1 in the ferromagnetic phases, $\cos \frac{2\pi}{5} \simeq 0.309$ in the ferrimagnetic phases, $\cos \frac{4\pi}{5} \simeq -0.81$ in the anti-ferrimagnetic phase and to vanish in the paramagnetic phase. On figure 4, the two ferromagnetic phases appear as red, i.e. $e \simeq 1$, and at the expected location. In the two phases of partial magnetic order previously

observed, the two-site correlation e is compatible with $e \simeq 0.309$, in agreement with the interpretation of these phases as ferrimagnetic. The anti-ferrimagnetic phase is now better resolved than with A_1 . The different contour lines are indeed closer to each other. As a consequence, defining the phase boundary with the paramagnetic phase as the contour line $e = e_{PB} = 0.4$ leads to a more stable result upon small variations of e_{PB} than with A_1 . The discrepancy with earlier Monte Carlo simulations is confirmed.

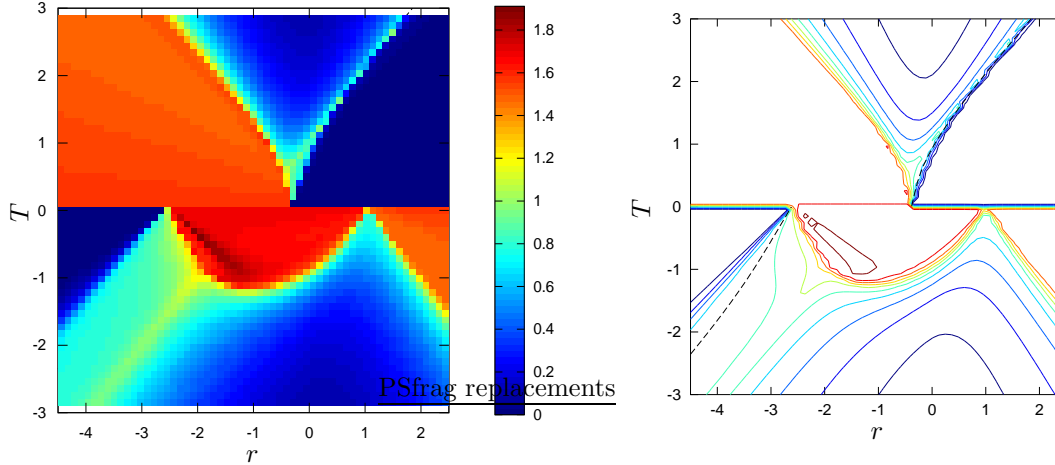


Figure 5. Entanglement entropy $S(L/2)$ versus $r = J_2/J_1$ and $T = 1/J_1$ for a lattice size $L = 128$ obtained by DMRG with 325 states and 6 sweeps. On the right, contour plot of the same data. The dashed line is the self-dual line of the model.

Finally, probably the most stable locations of the phase boundaries are given by the entanglement entropy $S(L/2)$ in the ground state of one half of the system with the second half. The Hilbert space being decomposed as a tensor product of the left and a right Hilbert spaces, i.e. $\mathcal{H} = \mathcal{H}_L \otimes \mathcal{H}_R$, the entanglement entropy is defined as the average of the logarithm of the reduced density matrix of one of the halves [25]:

$$S(L/2) = -\text{Tr}_{\mathcal{H}_L} \rho_L \ln \rho_L \quad (14)$$

where

$$\rho_L = \text{Tr}_{\mathcal{H}_R} \rho = \text{Tr}_{\mathcal{H}_R} |\psi_0\rangle\langle\psi_0| \quad (15)$$

and $|\psi_0\rangle$ is the ground-state of the transfer matrix. Since the computation and the diagonalization of the reduced density matrix is required at every iteration of the DMRG algorithm, the entanglement entropy is easily obtained. $S(L/2)$ is presented on figure 5. Even though, the nature of the phases cannot be identified solely with the entanglement entropy, the phase boundaries are much better defined than with more traditional observables. The phase diagram discussed before is confirmed.

However, the critical phase between the ferromagnetic and paramagnetic phases cannot be identified anymore, neither in the upper half-plane nor in the lower one. Moreover, a bump of $S(L/2)$ is observed along a line $r \simeq -1 - T$ in the paramagnetic phase of the lower half-plane. A bump in the specific heat was observed in earlier Monte Carlo simulations but for larger values of r . However, as will be discussed

in the following, the entanglement entropy is hampered by large Finite-Size effects. Therefore, these bumps may have the same origin. In Ref. [17], the bump in specific heat was interpreted as a phase boundary between the paramagnetic phase and the anti-ferrimagnetic critical phase. The DMRG data previously discussed exclude this possibility.

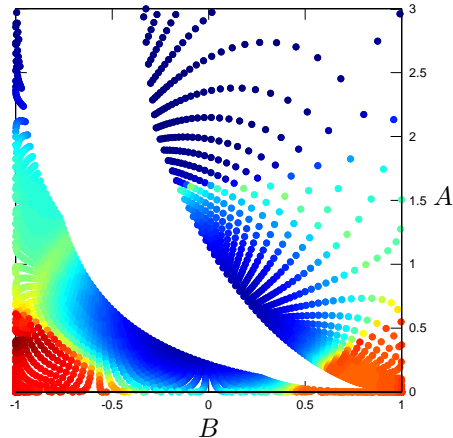


Figure 6. Entanglement entropy using the parameters A et B introduced by M. den Nijs.

On figure 6, the entanglement entropy is plotted versus the two parameters A and B introduced by den Nijs. The anti-ferrimagnetic and ferrimagnetic phases are easily distinguished at respectively the left and right corners. In contrast, the ferromagnetic phases are almost impossible to see. Nevertheless, the visible part of the phase diagram is very similar to the one depicted schematically on Fig. 1 of Ref. [16]. However, the location of the transition lines is slightly different. Based on the assumption that the mechanism behind these transitions is the melting of the string binding the q -vortices, den Nijs predicted that the transitions should occur at $A = \sqrt{2} - 1$ when $B = \pm 1$. Our numerical data show a transition at higher values $A \simeq 0.6$.

3.2. Finite-size scaling of entanglement entropy and free energy

In non-critical phases, local degrees of freedom are expected to be entangled over a distance of the order of the correlation length ξ . Therefore, the entanglement entropy is finite, $S \sim \ln \xi$, and does not depend on the lattice size L as long as $L > \xi$. At critical points or in critical phases, the correlation length becomes infinite and the entanglement entropy grows with the lattice size as $S \sim \kappa \ln L$. In conformal field theories (CFT), the prefactor κ is universal and proportional to the central charge c [26, 27]. For periodic boundary conditions, $\kappa = c/3$ while $\kappa = c/6$ for open ones.

On figure 7, the entanglement entropy $S(L/2)$ is plotted for four different couplings $J_1 = 1/T$ versus $r = J_2/J_1$. The curves for $L = 128$ correspond to horizontal sections of figure 5. One can clearly distinguish regions where the curves corresponding to different lattice sizes fall on top of each other. These regions of L -independent entanglement entropy are therefore non-critical. In contrast, three

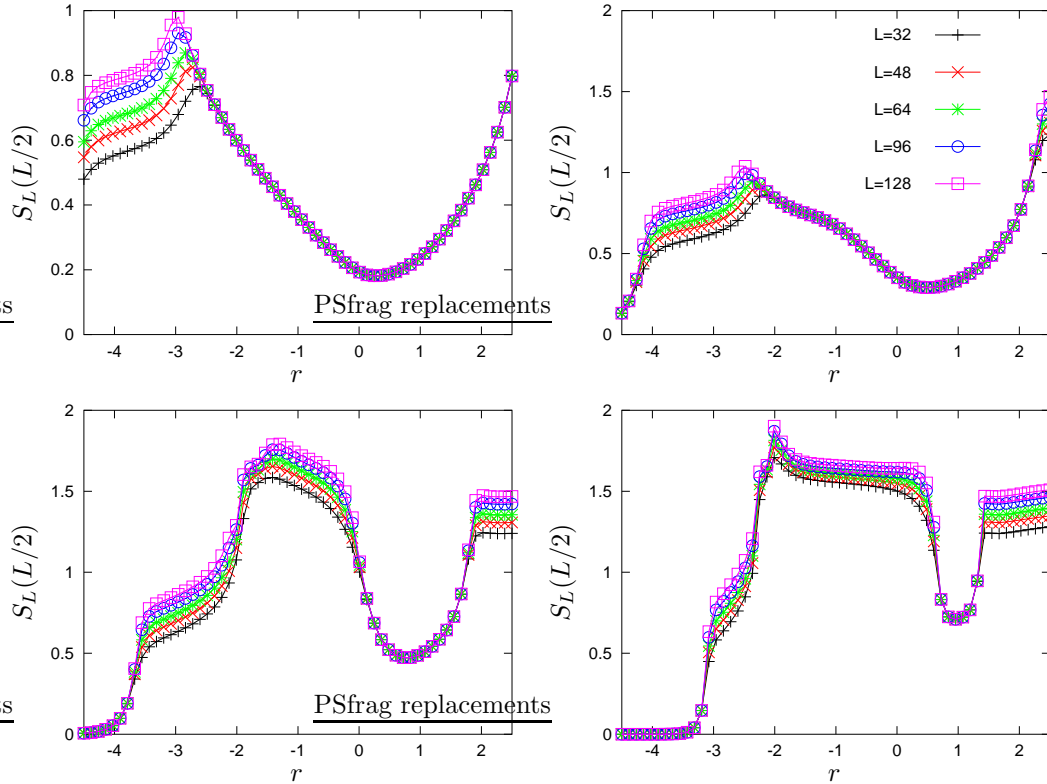


Figure 7. Entanglement entropy versus $r = J_2/J_1$. The different graphs correspond to $T = 1/J_1 \simeq -1.983$ (top left), -1.475 , -0.966 and -0.458 (bottom right).

critical phases are observed, in agreement with the discussion of the previous section. At $T \simeq -1.983$, only the critical phase that we conjectured to exist between the ferromagnetic and paramagnetic phases, is observed. This critical phase is bounded by a peak whose location corresponds precisely to the yellow stripe observed on figure 5. However, this peak is strongly shifted to smaller values of r as the lattice size is increased. Entanglement entropy being a non-local quantity, it is indeed more sensitive to boundaries than local observables. Therefore, while entanglement entropy was useful to enlighten the critical nature of this phase, its boundaries are probably more accurately given by magnetization-magnetization autocorrelation A_1 for example. As $T = 1/J_1$ is decreased, a second critical phase is observed on figure 7, corresponding to the anti-ferrimagnetic phase. Finally, at $T \simeq -0.458$, the ferrimagnetic critical phase is observed on the right of the figure.

On figure 8, the entanglement entropy $S(L/2)$ is plotted versus $\ln L$ at different points of the phase diagram, all of them belonging to critical phases. As expected, the behavior is very nicely linear with a slope in the range $0.1620(7)$ ($T \simeq -0.458$, $r \simeq -2.839$) to $0.1649(7)$ ($T \simeq -1.475$, $r \simeq -3.669$). These values are slightly below but close to the conformal prediction $\kappa = c/6$ with a central charge $c = 1$. This result is consistent with the existence of a mapping of the ground state in the ferrimagnetic and anti-ferrimagnetic critical phases onto a Solid-On-Solid model, i.e. a

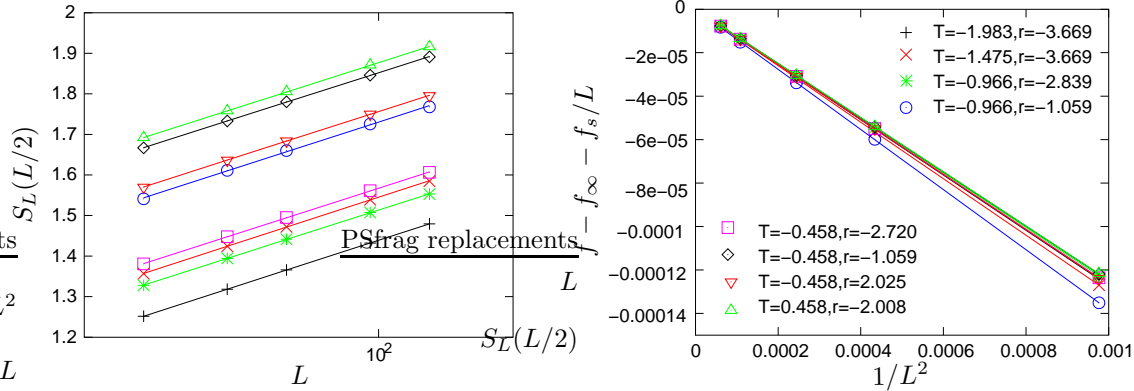


Figure 8. On the left, entanglement entropy $S_L(L/2)$ versus L in a semi-logarithmic scale at different points of the phase diagram. The lines are linear fits. On the right, free energy density after the removal of the thermodynamic limit f_∞ and the surface free energy f_s . The symbols are the same on the two figures.

Gaussian theory, as discussed in the second section. Note that the data presented on figure 8 result from additional numerical calculations with open boundary conditions, i.e. without boundary magnetic fields, as required by conformal theory. In presence of boundary fields, the prefactor κ would be slightly smaller in the anti-ferrimagnetic phase.

The same information can be extracted from the Finite-Size Scaling of the free energy density. In presence of open boundary conditions, the latter is predicted by CFT to behave as

$$f(L) = f_\infty + \frac{f_s}{L} + \frac{\kappa'}{L^2} + \mathcal{O}(L^{-3}) \quad (16)$$

where f_s is a surface free energy density and $\kappa' = \pi c/24$. This behavior is clearly observed and a parabolic fit gives the three parameters f_∞ , f_s and κ' with a good accuracy. On figure 8, the quantity $f(L) - f_\infty - f_s/L$, where $f(L)$ corresponds to the numerical data while f_∞ and f_s result from the fit, is plotted versus $1/L^2$. The nice linear behavior that is observed shows that the higher-order terms in $1/L$ can be safely neglected. κ' is found in the range -0.1246 ($T \simeq -0.458$, $r \simeq -2.008$) to -0.1383 ($T \simeq -0.966$, $r \simeq -1.059$). The corresponding central charges are in the range $0.952 - 1.056$.

3.3. Berezinskii-Kosterlitz-Thouless transitions in the AF regime

In this section, the location of the BKT transition between the critical phase and the paramagnetic phase is more precisely determined. Despite the lack of spontaneous symmetry breaking in the critical phase, an order parameter, the helicity modulus Υ , can be defined [28]. Twisting boundary conditions are imposed to the system to induce a spin wave. The helicity modulus is related to the variation of free energy density as

$$\Upsilon = L^2 \left(\frac{\partial^2 f}{\partial \Delta^2} \right)_{\Delta=0} \quad (17)$$

where Δ is the angle difference imposed to spins at the left and right boundaries. In the XY model, whose Hamiltonian is $-J \sum_{\langle i,j \rangle} \cos(\theta_i - \theta_j)$, the helicity modulus is expected to display a jump equal to the stiffness J at the BKT transition in the thermodynamic limit. In practise, this quantity is computed numerically by imposing different orientations of the magnetic field at the two boundaries. In the case of the $\mathbb{Z}(q)$ model, the Hamiltonian (??) is replaced by

$$-\beta H_{\text{BC}} = \cos \frac{2\pi}{q} \sigma_1 + \cos \frac{2\pi}{q} (\sigma_L - \Delta). \quad (18)$$

where Δ is a now discrete quantity. The free energy density $f(\Delta)$ is computed for $\Delta = 0$ and 1 and the helicity modulus is estimated as

$$\Upsilon = \frac{2L^2}{(2\pi/q)^2} (f(0) - f(1)). \quad (19)$$

This procedure has been shown to give the correct helicity modulus in the case of the 5-state Potts model, i.e. $J_2 = 0$ here [29]. It should therefore extend to the BKT transition between the critical phase and the ferromagnetic and paramagnetic phases. In the case of the ferrimagnetic and anti-ferrimagnetic phases, the boundary fields introduce a frustration at both boundaries. The contribution of the two additional surface free energies should however cancel in the definition of the helicity modulus.

The helicity modulus Υ is plotted on figure 9 versus $r = J_2/J_1$ for four different temperatures. For $T = 1/J_1 \simeq -1.983$ and -1.475 , the curves are typical of a model undergoing a BKT transition and very similar to those observed for the 5-state clock model [29]. As the lattice size L is increased, the curves become steeper and steeper, as expected for a quantity displaying a jump in the thermodynamic limit. To estimate the location of the transition, the helicity modulus is fitted linearly in the region of sharpest variation. Those fits are represented on figure 9. As expected, the slope increases with the lattice size. The intercept with the x -axis is then extrapolated in the limit $L \rightarrow +\infty$. The BKT transition points are estimated to be located at $r_{\text{BKT}} = -3.29(21)$ for $T \simeq -1.983$, $-2.77(13)$ for $T \simeq -1.475$, $-2.24(28)$ for $T \simeq -0.966$, and $-1.97(12)$ for $T \simeq -0.458$.

For $T \simeq -0.458$, the anti-ferrimagnetic and ferrimagnetic critical phases appear as a bump in the helicity modulus Υ . However, we do not know how to interpret this to extract useful informations since the topological transition is not of BKT-type in these cases.

3.4. Autocorrelation functions

In this section, the correlation functions are shown to decay algebraically in all critical phases and an associated critical exponent is estimated. On figure 10, the absolute value of spin-spin autocorrelation functions

$$C_{\sigma\sigma}(t) = |\langle \cos \frac{2\pi}{q} [\sigma_{L/2}(t) - \sigma_{L/2}(0)] \rangle| \quad (20)$$

and energy-energy autocorrelation functions

$$C_{ee}(t) = \langle e(t)e(0) \rangle - \langle e \rangle^2 \quad (21)$$

with

$$e(t) = \cos \frac{2\pi}{q} (\sigma_{L/2}(t) - \sigma_{L/2+1}(t)) \quad (22)$$

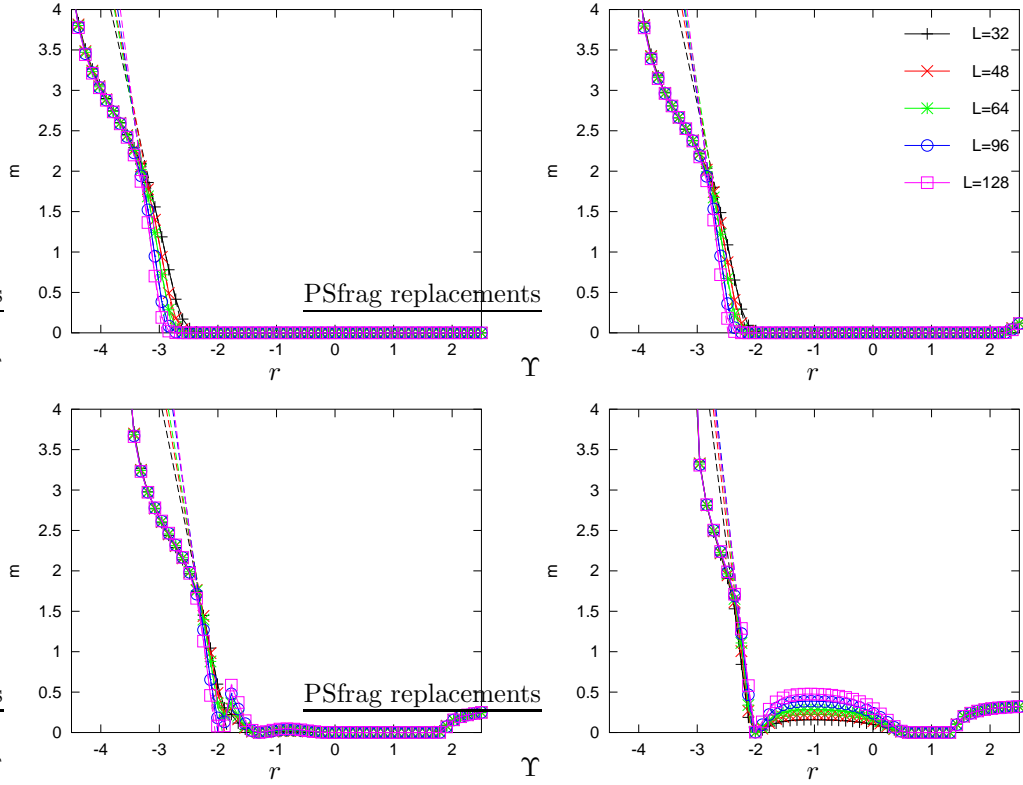


Figure 9. Helicity modulus Υ versus $r = J_2/J_1$. The different graphs correspond to $T = 1/J_1 \simeq -1.983$ (top left), -1.475 , -0.966 and -0.458 (bottom right). The different curves correspond to different lattice sizes as indicated in the legend. The dashed lines are linear fits of the helicity modulus in the region of sharpest variation.

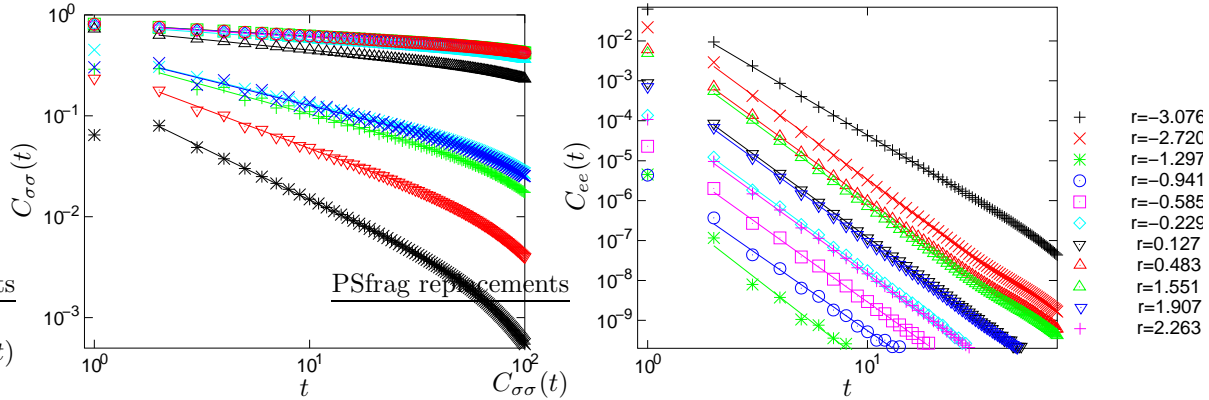


Figure 10. On the left, absolute value of the spin-spin correlation functions at different values of r and at $T = 1/J_1 \simeq -0.458$. The lines are log-log fits. On the right, energy-energy correlation functions at the same values of r and T .

are plotted for $T \simeq -0.458$ and for values of r that correspond to points of the phase diagram in critical phases. The absolute value was introduced because in the anti-ferrimagnetic phase, the spin-spin correlation function is oscillating. For all points considered, a nice algebraic decay is observed, at least for small times $t \lesssim 30$ due to the finite size of the system. For larger times, an exponential decay is recovered.

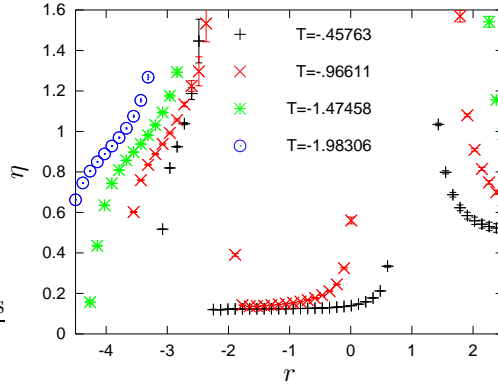


Figure 11. Critical exponent η , computed from a log-log fit of spin-spin autocorrelation functions, versus r . The different symbols correspond to different values of T . To exclude the points of the phase diagram in non-critical phases (ferromagnetic and paramagnetic), two criterions have been used: the entanglement entropy $S_L(L/2)$ was required to be larger than 0.7 and r to be outside the range $[r_{\text{BKT}}(T); -2]$ where $r_{\text{BKT}}(T)$ is the location of the BKT transition as given by the jump of the helicity modulus.

The critical exponent η was computed by a log-log fit of spin-spin autocorrelation functions. As can be seen on figure 11, three distinct behaviors are observed. First, in the critical phase lying between the ferromagnetic and paramagnetic phases, the exponent η grows rapidly as r is increased. It seems to vanish at the first BKT transition, i.e. at the boundary of the ferromagnetic phase. The rapid variation of η with r makes difficult the estimation of its value along the second BKT transition line, i.e. between the critical and paramagnetic phase. The exponent takes a value in the range 1.3–1.5 and may be constant along the BKT transition line. In the anti-ferrimagnetic phase, the exponent η displays a plateau, clearly seen for $T \simeq -0.457$. The estimate vary from 0.1232 at $r \simeq -1.9$ to 0.1262 at $r \simeq -0.7$. It is tempting to conjecture that the exponent η takes the rational value $1/16$, i.e. half of the exponent of the Ising model, in all points of the anti-ferrimagnetic phase. However, at the right boundary of the anti-ferrimagnetic phase an increase of η is observed. It may not be physical but due to finite size effects. For $T \lesssim -1$, there is no anti-ferrimagnetic phase anymore. Finally, in the ferrimagnetic phase, the exponent η decreases with r . It is not possible to say whether η takes the same value along the topological transition line or not.

An exponent $\eta_e = 2x_e$ have also been computed by a log-log fit of the energy-energy autocorrelation functions. However, it is much noisier than η and we will not draw any conclusion about it.

4. Conclusions

The phase diagram of the 5-state $\mathbb{Z}(q)$ model has been determined numerically using Density Matrix Renormalization Group and compared to earlier Monte Carlo simulations. In the quadrant $T = 1/J_1 < 0$ and $r = J_2/J_1 < 0$ where the two interactions are frustrated, a new phase diagram is proposed. The critical anti-ferrimagnetic phase is finite and does not share any boundary with the ferromagnetic phase, apart from one point in the limit $T \rightarrow 0^-$. At the boundary of the ferromagnetic phase lies a critical phase. Similarly to what happens when $T, r > 0$, the system undergoes two successive BKT transitions when going from the paramagnetic phase to the ferromagnetic one. This phase diagram is supported by the behavior of the entanglement entropy and the helicity modulus. It contradicts earlier Monte Carlo simulations but is in agreement with den Nijs' predictions.

We have however not directly tested the assumptions that led den Nijs to his predicted phase diagram. It would be interesting to give direct numerical evidence that the melting of the string binding the q -vortices is indeed responsible for the phase transitions of the anti-ferrimagnetic and ferrimagnetic phases to the paramagnetic phase.

References

- [1] V. L. Berezinskii. *Zh. Eksp. Teor. Fiz.*, **61** 1144, (1971).
- [2] J. M. Kosterlitz and D. J. Thouless *J. Phys. C: Solid State Physics*, **6** 1181, (1973).
- [3] J. Villain *J. Phys. C: Solid State Physics* **10** 1717 (1977)
- [4] H.W.J. Blöte, M.P. Nightingale, X.N. Wu and A. Hoogland *Phys. Rev. B* **43** 8751 (1991) ;
H.W.J. Blöte and M.P. Nightingale *Phys. Rev. B* **47** 15046 (1993).
- [5] D.P. Foster, C. Gérard and I. Puha *J. Phys. A* **34** 5183 (2001)
- [6] J. Villain *J. Phys. C* **10** 4793 (1977)
- [7] M. Quartin and S.L.A de Queiroz *J. Phys. A: Math. Gen.* **36** 951 (2003)
- [8] C. Ding, H.W.J. Blöte and Y. Deng [arXiv:1508:04538](https://arxiv.org/abs/1508.04538) (2015)
- [9] W. Selke, *Phys. Rep.* **170** 213 (1988).
- [10] M. den Nijs *Phys. Rev.* **31**, 266 (1985).
- [11] D.H. Lee and G. Grinstein *Phys. Rev. Lett.* **55**, 541 (1985).
- [12] M. Dian and R. Hlubina *Phys. Rev. B* **84**, 224420 (2011).
- [13] F.C. Poderoso, J.J. Arenzon and Y. Levin *Phys. Rev. Lett.* **106**, 067202 (2011).
- [14] G.A. Canova, Y. Levin and J.J. Arenzon *Phys. Rev. E* **89** 012126 (2014).
- [15] J.V. José, L.P. Kadanoff, S. Kirkpatrick, and D.R. Nelson *Phys. Rev. B* **16**, 1217 (1977).
- [16] M. den Nijs *Phys. Rev. B* **31**, 266 (1985).
- [17] V.L.V. Baltar, G.M. Carneiro, M.E. Pol, and N. Zagury *J. Phys. A: Math. and Gen.* **18** 2017 (1985).
- [18] K. Rouidi and Y. Leroyer *Phys. Rev. B* **45** 1013 (1992).
- [19] R. B. Potts. *Mathematical Proceedings of the Cambridge Philosophical Society*, **48** 106, (1952).
- [20] S. Elitzur, R.B. Pearson and J.B. Shigemitsu *Phys. Rev. D* **19** 3698 (1979).
- [21] V.A. Fateev, and A.B. Zamolodchikov *Phys. Lett. A* **92**, 37 (1982).
- [22] E. H. Lieb *Phys. Rev.* **162** 162 (1967).
- [23] S. R. White *Phys. Rev. Lett.*, **69** 2863, (1992) ; S. R. White *Phys. Rev. B*, **48** 10345, (1993).
- [24] U. Schollwöck *Rev. Mod. Phys.*, **77** 259, (2005).
- [25] L. Amico, R. Fazio, A. Osterloh, and V. Vedral (2008) *Rev. Mod. Phys.* **80**, 517.
- [26] G. Vidal, J.I. Latorre, E. Rico, and A. Kitaev (2003) *Phys. Rev. Lett.* **90**, 227902.
- [27] P. Calabrese and J. Cardy (2004) *J. Stat. Mech.: Theory Exp.* P06002.
- [28] M. E. Fisher, M. N. Barber, and D. Jasnow. *Phys. Rev. A*, **8** 1111, (1973).
- [29] C. Chatelain *J. Stat. Mech.: Theory Exp.* P11022 (2014).